Supporting Information for

Crossing the Dimensional Divide with Optoelectronic Tweezers: Multicomponent Light-driven Micromachines with Motion Transfer in Three Dimensions

Gong Li *et al.*

*Corresponding author. Email: Jiafang Li, jiafangli@bit.edu.cn; Shuailong Zhang, shuailong.zhang@bit.edu.cn

This PDF file includes:

Supplementary Text
Figs. S1 to S8
Tables S1

Other Supplementary Materials for this manuscript include the following:
Movies S1 to S8

Supplementary Text

Experimental setup

The OET setup comprises a Digital Micromirror Devices (DMD) -based pattern illuminator (Mightex Polygon 1000G, 625 nm 1100 mW LED source, Toronto, Canada) interfaced with an upright optical microscope (OLYMPUS BX63 microscope integrated with Märzhäuser Scan Plus 100 × 100 motorized stage), using a ×10 (UPLFLN10×2, NA0.3, Japan), ×20 (MPLFLN20×, NA0.45, Japan) or ×50 (MPLFLN50×, NA0.80, Japan) objective, respectively (and no optical-induced heating was observed for these conditions). Finally, the resolution of optical patterns (defined as the lateral distance between two distinguishable optical points generated by adjacent DMD pixels) formed in this system are 0.8 and 0.5 μm for the ×10 objective and ×20 objective, respectively. OET devices were similar to those reported previously (*1-4*), consisting of a 30 µL fluidic chamber sandwiched between two glass plates separated by a 225 µm spacer. The plates are coated with a thin layer of indium tin oxide (ITO, Gologlass, Luoyang, China), and the bottom plate is formed from an ITO-coated glass slide, with the ITO layer coated with 1 µm thick a-Si:H (see Fig. 1), deposited by plasma enhanced chemical vapor deposition (Oxford Instruments Plasmalab 180 ICP-CVD system) from silane gas (30 sccm) at 250 °C with 10 W input power at 10 mTorr pressure. AC potentials (5–30 V_{pp}, 10–30 kHz, sine waves) used to drive the OET device were supplied by a function generator (RIGOL DG1022Z) and an amplifier (Thurlby Thandor Instrument WA301). At these frequencies, the sign of the real part of the Clasius–Mossotti factor is negative for the micro-gear and liquid media (aqueous solutions with conductivity <30 mS/m) used here (*4*). When not specified otherwise, the OET bias was set to 20 V at 10 kHz. In this frequency regime, DEP is the dominant force relative to AC electroosmosis (*5*). SEM images were collected using an environmental SEM (QUANTA FEG 250 ESEM), with a pressure of 80 Pa and an electron beam with 15 keV energy and 3 nm spot size. 3D profiles were measured by an optical profilometer (Bruker Contour GT-K).

Microfabrication

Micro-gears were formed from SU-8 2015 (MicroChem, USA) at the University of Toronto and Beijing Institute of Technology's cleanroom facility using methods similar to those reported previously (*6,7*). Briefly, 1 mL Omnicoat (MicroChem, USA) was spin-coated on top of a 4-inch silicon wafer (2000 r.p.m. for 30 s), followed by soft baking at 200 °C for 1 min. After cooling the silicon wafer to room temperature, 4 mL SU-8 2015 was spin-coated at 1300 r.p.m. (for ~30-µm-thick micro-gears) for 30 s atop the silicon substrate, followed by soft baking at 65 °C for 3 min and 95 °C for 8 min. Next, a mask aligner (URE-2000/35) was used to illuminate the substrates (exposure energy: 9 mJ/cm^2 for 10 s) through a photomask to selectively photo-crosslink the SU-8. After postexposure baking (65 °C for 2 min and 95 °C for 7 min) and developing in SU-8 developer (8 min), the substrates were air-dried with pressurized nitrogen. The substrates were then immersed in Remover PG (Microchem, USA) to dissolve the Omnicoat (3 min under gentle agitation) and to lift the photo-cured SU-8 micro-gears into suspension. The suspension was collected into a 15 mL tube and centrifuged at 14,500 × g for 30 s, the supernatant was removed, and the micro-gears were resuspended in deionized (DI) water (prepared by MicroPure UF/UV, Thermo Scientific, USA) containing 0.05% volume ratio of Tween-20 (P9416, Sigma). The centrifuge/resuspension process was repeated three times, after which the suspensions were stored at room temperature until use. Immediately prior to use, each micro-gear suspension was gently vortexed, and an aliquot (30 µL) was loaded into the chamber of an OET device.

Mechanical supports were printed via 2PP using IP-S photoresist (Nanoscribe GmbH, Germany) on the top plate of OET chip by a direct laser writing system (Photonic Professional GT2, Germany). During the printing, the lateral distance of two adjacent laser scanning lines within the x-y layer is 0.3 µm, and the moving step of laser on the z-axis is 0.5 µm.

Micro-gear dimensions

Supplementary Fig. S1A shows the Scanning Electron Microscope (SEM) image of a standard micro-gear used in this work, which has eight teeth and a micro-hole in the center. Supplementary Fig. S1B shows the SEM image of a micro-gear array. Supplementary Figs. S1C and S1d show the measured 3D profiles of the micro-gears, in which the thickness is indicated in a heat map (blue = low, red = high). The width and thickness of the micro-gears were measured to be approximately 200 μm and 30 μm, respectively.

Theory of OET

For a micro-object in an OET system, it experiences DEP force which can be expressed as(*8*):

$$F_{DEP} = p \cdot \nabla E \tag{1}$$

in which p represents the dipole momentum and ∇E represents the gradient of the electric field.

Based on the simulation models, integral operations for complex shapes and surfaces will be easier to perform. The DEP force applied to the micro-gear can be obtained by integrating the Maxwell stress tensor (MST) over the surface of the micro-gear(*9,10*), which could be expressed as:

$$F_{DEP} = \oiint T \cdot \vec{n} dS \tag{2}$$

where T represents the MST on the micro-gear surface, $\vec{n}$ represents the unit vector normal to the micro-gear surface, dS represents the area element of the micro-gear surface.

Similar to the calculation of the DEP force, the DEP torque can be calculated by surface integration, which could be expressed as:

$$T_{DEP} = \oiint \vec{r} \times T \cdot \vec{n} dS \tag{3}$$

where $\vec{r}$ represents the vector from the rotation axis to dS.

To facilitate numerical calculations, the rotation axis is used as the coordinate axes and the center of the rotation axis is used as the origin of the model coordinates. The three axes XYZ are perpendicular to each other and any of the axis can be expressed by the cross product of two other axes. Therefore, when the rotation axis is the X-axis, the DEP torque can be calculated as follows:

$$T_{DEP} = \oiint (\vec{y} \times T \cdot \overrightarrow{n_z} - \vec{z} \times T \cdot \overrightarrow{n_y}) dS \tag{4}$$

where $\vec{y}$ represents the Y-axis component of the distance vector (from the rotation axis to dS), $\overrightarrow{n_z}$ represents the Z-axis component of the unit vector normal to dS, $\vec{z}$ represents the Z-axis component of the distance vector (from the rotation axis to dS), $\overrightarrow{n_y}$ represents the Y-axis component of the unit vector normal to dS. Moments of inertia for the micro-gear can be calculated via volume integration, and the density used for the volume integration was given in supplementary Table S1.

Modeling and numerical simulation

Simulation of the OET device: The simulation model of the OET device was constructed utilizing a 3D Alternating Current (AC) module within COMSOL Multiphysics 6.2 (COMSOL, Stockholm, Sweden). The thickness of the photoconductive layer (a-Si:H) and the liquid medium were set as 1 μm and 225 μm, respectively. A SU-8-based micro-gear, mirroring the dimensions utilized in experimental settings, was positioned 1 μm above the OET device's bottom surface. Regions of high conductivity corresponded to those illuminated by light in experimental observations. Comprehensive parameters including conductivity, permittivity, and others are provided in supplementary Table S1. Within the simulation model, the electric potential of the bottom surface was maintained at 25 V, while the top surface was grounded to 0 V. Furthermore, the AC frequency of the bias voltage was set at 10 kHz, in accordance with experimental conditions. The electric field, Maxwell Stress Tensor (MST), and charge distribution across the micro-gear surface were simulated by solving the continuity equation inherent to the model.

Simulation of micro-gears with two thicknesses: The thicknesses of the two micro-gears were set at 30 μm and 60 μm, respectively. To substantiate the assertion that thinner micro-gears are more prone to flipping, an illuminated region with a diameter of 400 μm was centered within the photoconductive layer. Variation of the X-coordinates of the micro-gears across the range of 0-350 μm was employed to simulate the flipping process. The DEP torque requisite for flipping the micro-gear was determined by integrating the cross product of the vector extending from the rotation axis to dS with the MST over the micro-gear's surface. Subsequently, the angular acceleration of the micro-gear's flipping motion was calculated by dividing the DEP torque by the moment of inertia of the micro-gear. In order to validate the hypothesis that thinner micro-gears exhibit greater ease of elevation, micro-gears of differing thicknesses were positioned at the model's center (on the XY plane), with heights ranging from 0.01 μm to 10 μm above the surface of the photoconductive layer (in the Z direction). The DEP force acting upon the micro-gears was simulated in the absence of light illumination, and the resulting accelerations of the micro-gears' elevation were computed by dividing the DEP lifting force by the respective mass of each micro-gear.

AC Simulation of the controllable flip of micro-gear: The illuminated area was derived through Boolean operations applied to two conformal cardioid rectangles, each centered at the midpoint of the photoconductive layer. The outer rectangle's dimensions were specified as 265 × 335 μm, while those of the inner rectangle were 85 × 245 μm. Positioned at 1 μm above the photoconductive layer in the Z direction, the micro-gear underwent scanning simulations conducted along the X-axis, with incremental steps of 1 μm, spanning a scanning range from -100 to 100 μm.

Fluid simulation for analysis of torque distribution in micro-gear trains

Due to the viscosity of the fluid, the micro-gear train gradually achieve motion stability when manipulated by OET. During this phase, the resistance encountered by the micro-gears matches the driving force, enabling the calculation of the micro-gear's dynamic torque through the assessment of viscous torque.

Given the same system input (same bias voltage, frequency, and beam intensity) of different experiments, the observed differences of the experimental results serve as the basis for further analysis of the micro-gear train systems. For the simulations, the parameters were set according to the measured experimental results. In addition, we simplify the micro-gear train model into single micro-gears, thereby facilitating the calculation of crucial parameters, such as the micro-gear's rotational direction and angular velocity.

The torque applied to the micro-gear as it rotates can be calculated by surface integrating the viscous forces. For example, the torque of a horizontally rotating micro-gear in the z-direction can be calculated using the following equation:

$$T_{Gear} = \oiint \left(\vec{x} \times T_{stress} \cdot \overrightarrow{n_y} - \vec{y} \times T_{Stress} \cdot \overrightarrow{n_x} \right) dS \tag{1}$$

where T_{stress} is the total viscous force across a basic micro-unit.

Supplementary Fig. S3A shows the 3D flow velocity distribution of a horizontal micro-gear rotating at 17 deg/s, which is the maximum rotational speed of a 3D micro-gear train. Fig. S3B shows the simulated 2D flow velocity distribution (top view) around the horizontally rotating micro-gear; Fig. S3C shows the simulated 2D flow velocity distribution across the cross-section

(YZ plane) of the horizontally rotating micro-gear. It was found that the intensity of the flow field is mainly concentrated near the surface of the rotating micro-gear. Furthermore, the intensity of the flow field near the bottom surface of the micro-gear is different from that of the top surface of the micro-gear, and the flow field gradient is stronger at the bottom surface of the micro-gear. The torque of the horizontally rotating micro-gear is calculated by surface integration of the viscous force, which was found to be 25859 pN·μm.

Supplementary Fig. S3D shows the 3D flow velocity distribution of a vertical micro-gear rotating at 17 deg/s. Fig. S3E shows the simulated 2D flow velocity distribution (side view) around the vertically rotating micro-gear; Fig. S3F shows the simulated 2D flow velocity distribution across the cross-section (XZ plane) of the vertically rotating micro-gear. It was found that the distribution of the flow field around the vertical micro-gear is more symmetric, and the torque was simulated to be 4523.2 pN·um. It can be found that the torque of vertically rotating micro-gear is lower than that of its horizontally rotating counterpart, indicating significant mechanical energy loss due to the friction between the micro-gear and its mechanical support.

Simulations of a single micro-gear as well as 2D micro-gear train were also performed using similar methods as to the 3D micro-gear train and the simulated torque results are presented in Fig. S4A.

References

1. S. Zhang, Y. Zhai, R. Peng, M. Shayegannia, A. G. Flood, J. Qu, X. Liu, N. P. Kherani, A. R. Wheeler, Assembly of topographical micropatterns with optoelectronic tweezers. *Adv. Opt. Mater.* **7**, 1900669 (2019).

2. S. Zhang, W. Li, M. Elsayed, J. Peng, Y. Chen, Y. Zhang, Y. Zhang, M. Shayegannia, W. Dou, T. Wang, Y. Sun, N. P. Kherani, S. L. Neale, A. R. Wheeler, Integrated assembly and photopreservation of topographical micropatterns. *Small.* **17**, 2103702 (2021).
3. M. A. Zaman, M. Wu, W. Ren, M. A. Jensen, R. W. Davis, L. Hesselink, Spectral tweezers: Single sample spectroscopy using optoelectronic tweezers. *Appl. Phys. Lett.* **124**, 071104 (2024)
4. M. A. Zaman, M. Wu, W. Ren, L. Hesselink, Impedance matching in optically induced dielectrophoresis: Effect of medium conductivity on trapping force. *Appl. Phys. Lett.* **125**, 051108 (2024)
5. J. K. Valley, A. Jamshidi, A. T. Ohta, H.-Y. Hsu, M. C. Wu, Operational Regimes and Physics Present in Optoelectronic Tweezers. *J. Microelectromech. Syst.* **17**, 342–350 (2008).
6. S. Zhang, M. Elsayed, R. Peng, Y. Chen, Y. Zhang, J. Peng, W. Li, M. D. Chamberlain, A. Nikitina, S. Yu, X. Liu, S. L. Neale, A. R. Wheeler, Reconfigurable multi-component micromachines driven by optoelectronic tweezers. *Nat. Commun.* **12**, 5349 (2021).
7. S. Zhang, E. Y. Scott, J. Singh, Y. Chen, Y. Zhang, M. Elsayed, M. D. Chamberlain, N. Shakiba, K. Adams, S. Yu, C. M. Morshead, P. W. Zandstra, A. R. Wheeler, The optoelectronic microrobot: A versatile toolbox for micromanipulation. *Proc. Natl. Acad. Sci. U.S.A.* **116**, 14823–14828 (2019).
8. R. Pethig, Review Article—Dielectrophoresis: Status of the theory, technology, and applications. *Biomicrofluidics* **4**, 022811 (2010).
9. X. Wang, X.-B. Wang, P. R. C. Gascoyne, General expressions for dielectrophoretic force and electrorotational torque derived using the Maxwell stress tensor method. *J. Electrostat* **39**, 277–295 (1997).
10. A. Al-Jarro, J. Paul, D. W. P. Thomas, J. Crowe, N. Sawyer, F. R. A. Rose, K. M. Shakesheff, Direct calculation of Maxwell stress tensor for accurate trajectory prediction during DEP for 2D and 3D structures. *J. Phys. D: Appl. Phys.* **40**, 71–77 (2007).

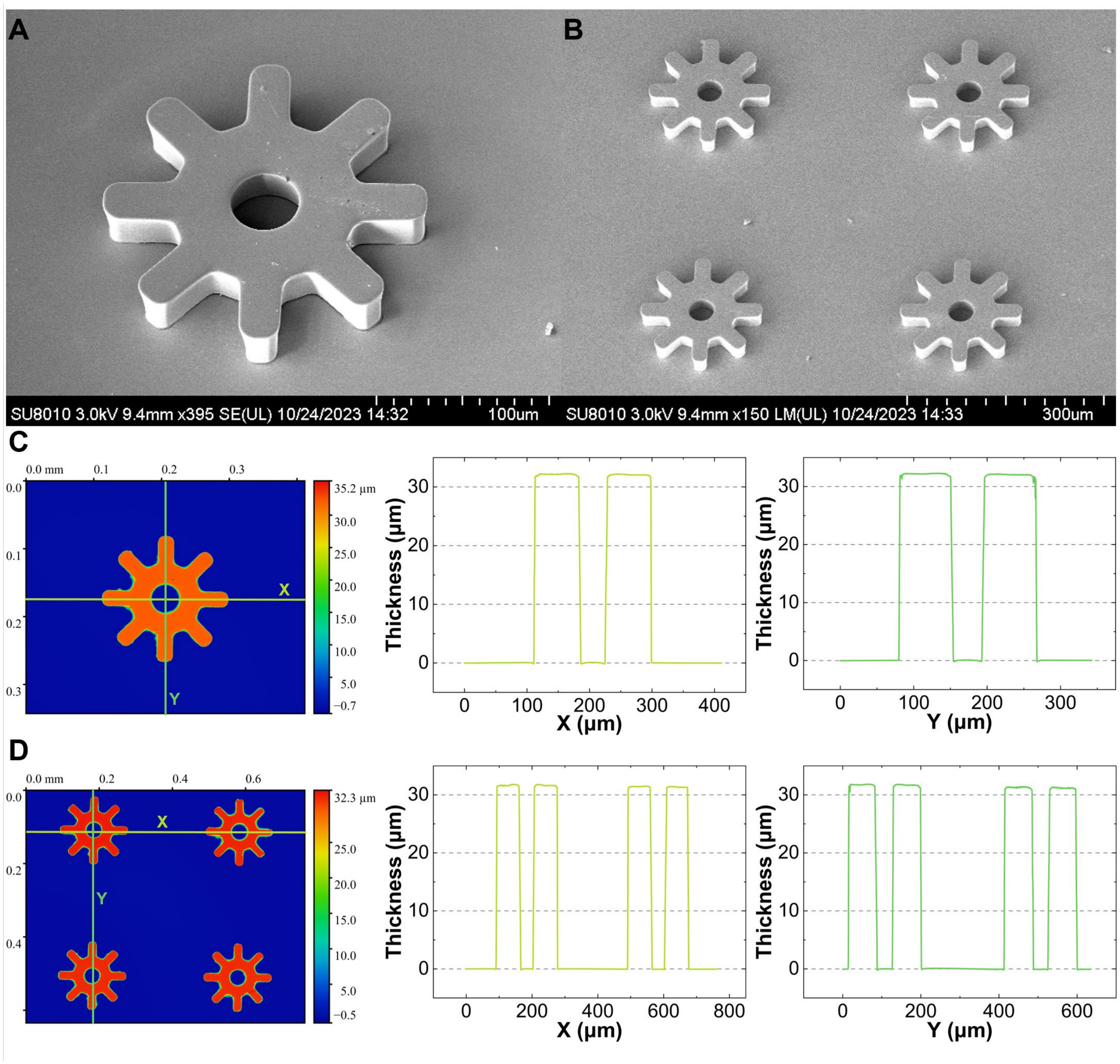

Fig. S1. Characterization of cogwheel micro-gears. (**A**) Scanning electron microscope (SEM) image of a micro-gear. (**B**) SEM image of a micro-gear array. (**C**) 3D Profile of a micro-gear (measured by Bruker Contour GT-K optical profilometer). (**D**) 3D Profile of a micro-gear array.

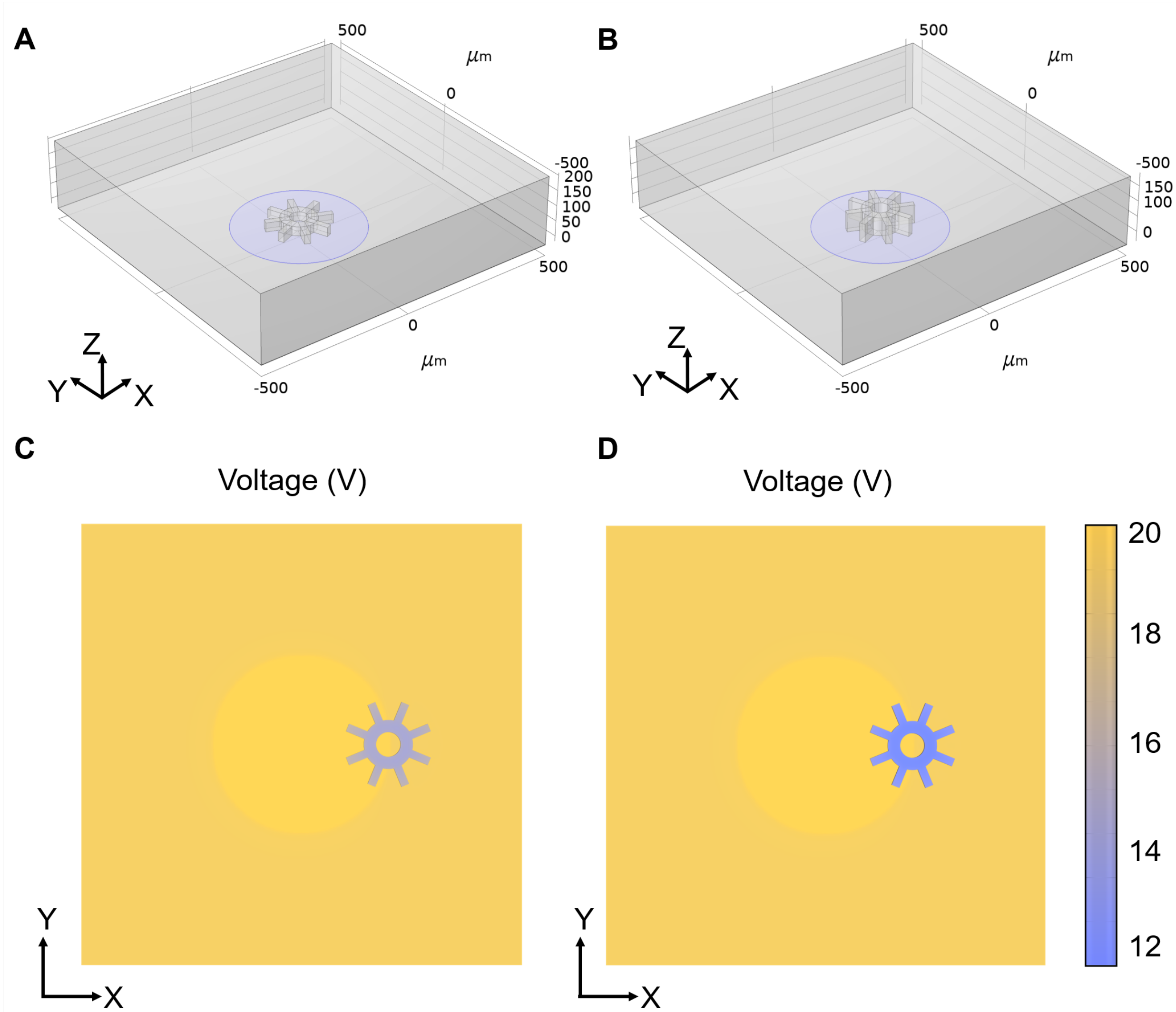

Fig. S2. Simulation model built to study the use of circular light pattern to flip micro-gear. Simulation model of (**A**) a 30-µm-thick micro-gear and (**B**) a 60-µm-thick micro-gear, both at the center of a circular light pattern (blue area indicates the light pattern, which has a diameter of 400 µm). Simulated potential distribution (top view) of (**C**) the 30-µm-thick micro-gear and (**D**) the 60-µm-thick micro-gear.

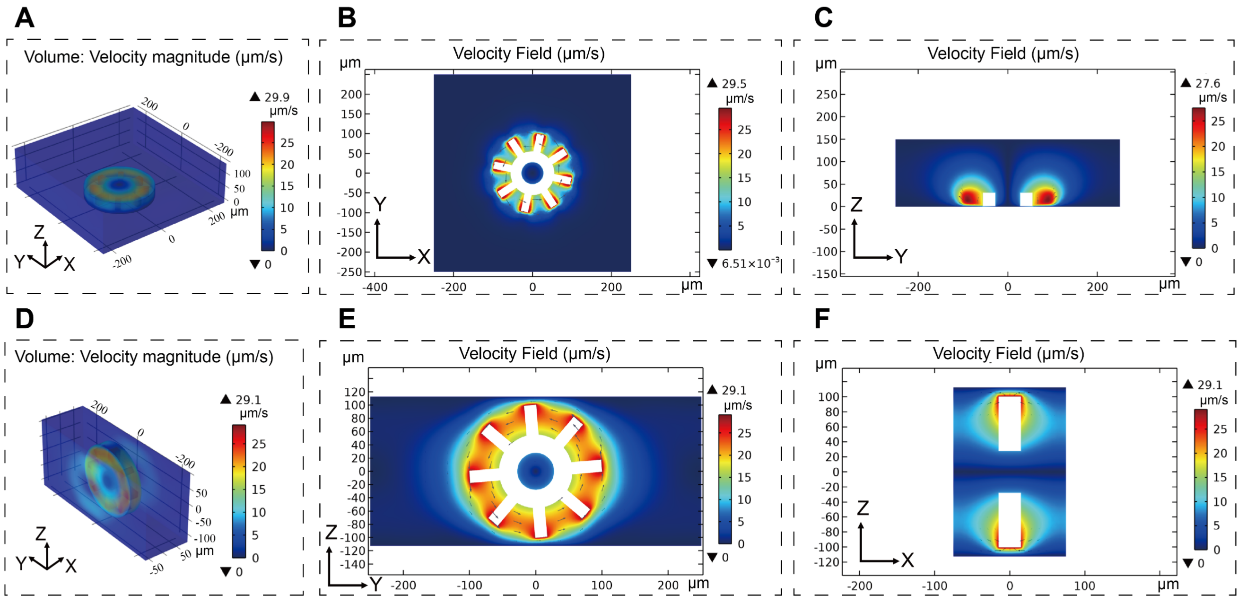

Fig. S3. Simulated flow field distribution of the 3D micro-gear train consisting of a horizontally rotating and a vertically rotating micro-gear. (**A**) Simulated 3D flow velocity distribution around a horizontally rotating micro-gear. (**B**) Simulated 2D flow velocity distribution (top view) around a horizontally rotating micro-gear. (**C**) Simulated 2D flow velocity distribution across the cross-section (YZ plane) of a horizontally rotating micro-gear. (**D**) Simulated 3D flow velocity distribution around a vertically rotating micro-gear. (**E**) Simulated 2D flow velocity distribution (side view) around a vertically rotating micro-gear. (**F**) Simulated 2D flow velocity distribution across the cross-section (XZ plane) of a vertically rotating micro-gear. More details of the simulation method are provided in Supplementary Note 2.

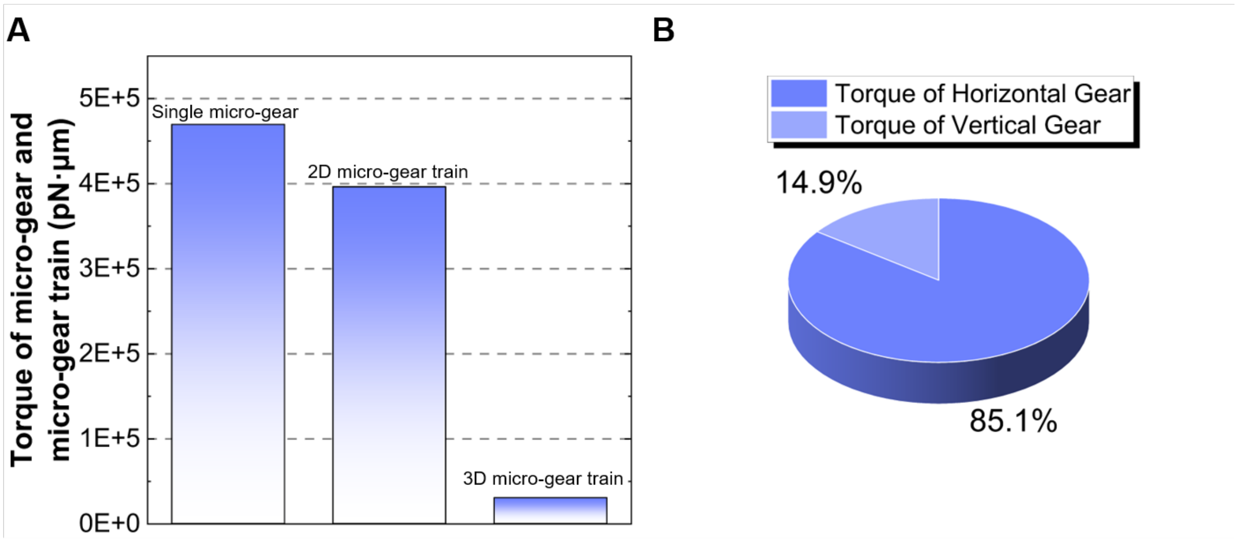

Fig. S4. Torque analysis for single micro-gear and micro-gear trains. (**A**) Comparison of torque of a horizontally rotating micro-gear, 2D micro-gear train and 3D micro-gear train. (**B**) Torque distribution within the 3D micro-gear train.

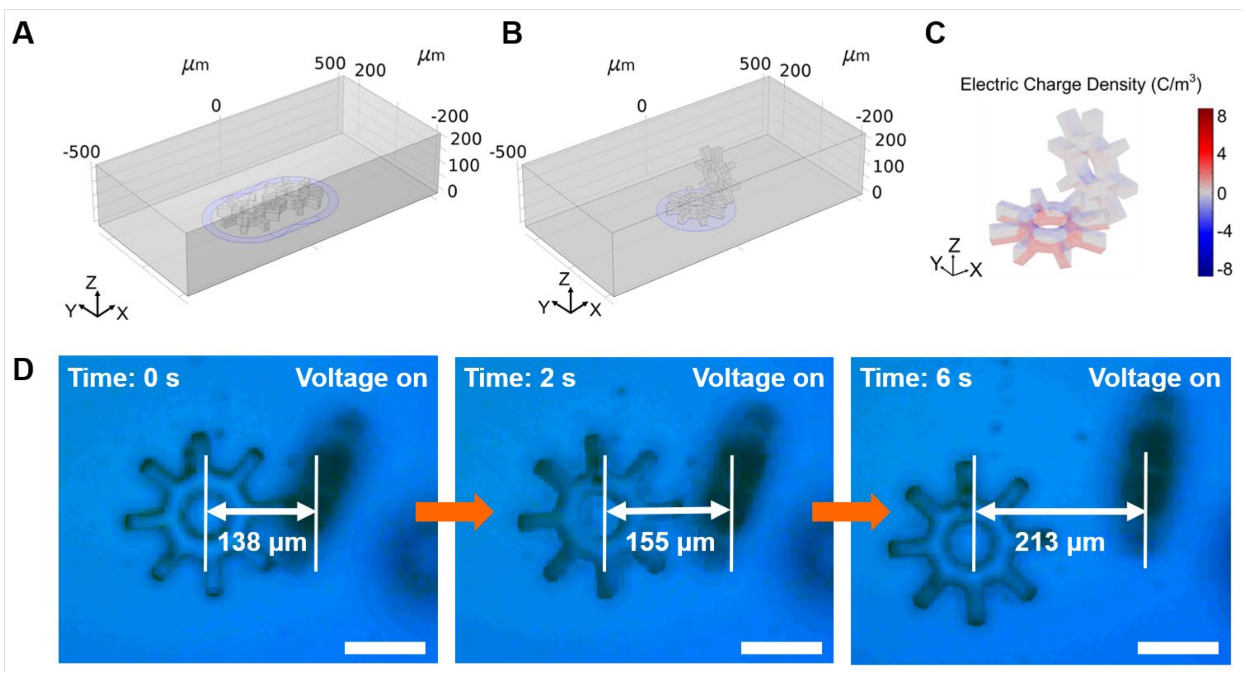

Fig. S5. Simulations of charge distribution in various micro-gear trains (20V, 10kHz). Simulation model of (**A**) 2D micro-gear train, and (**B**) 3D micro-gear train. (**C**) Simulated surface charge distribution in 3D micro-gear train system. (**D**) Repulsion between a horizontally lying micro-gear and an upright standing micro-gear (Scale Bar, 100 μm).

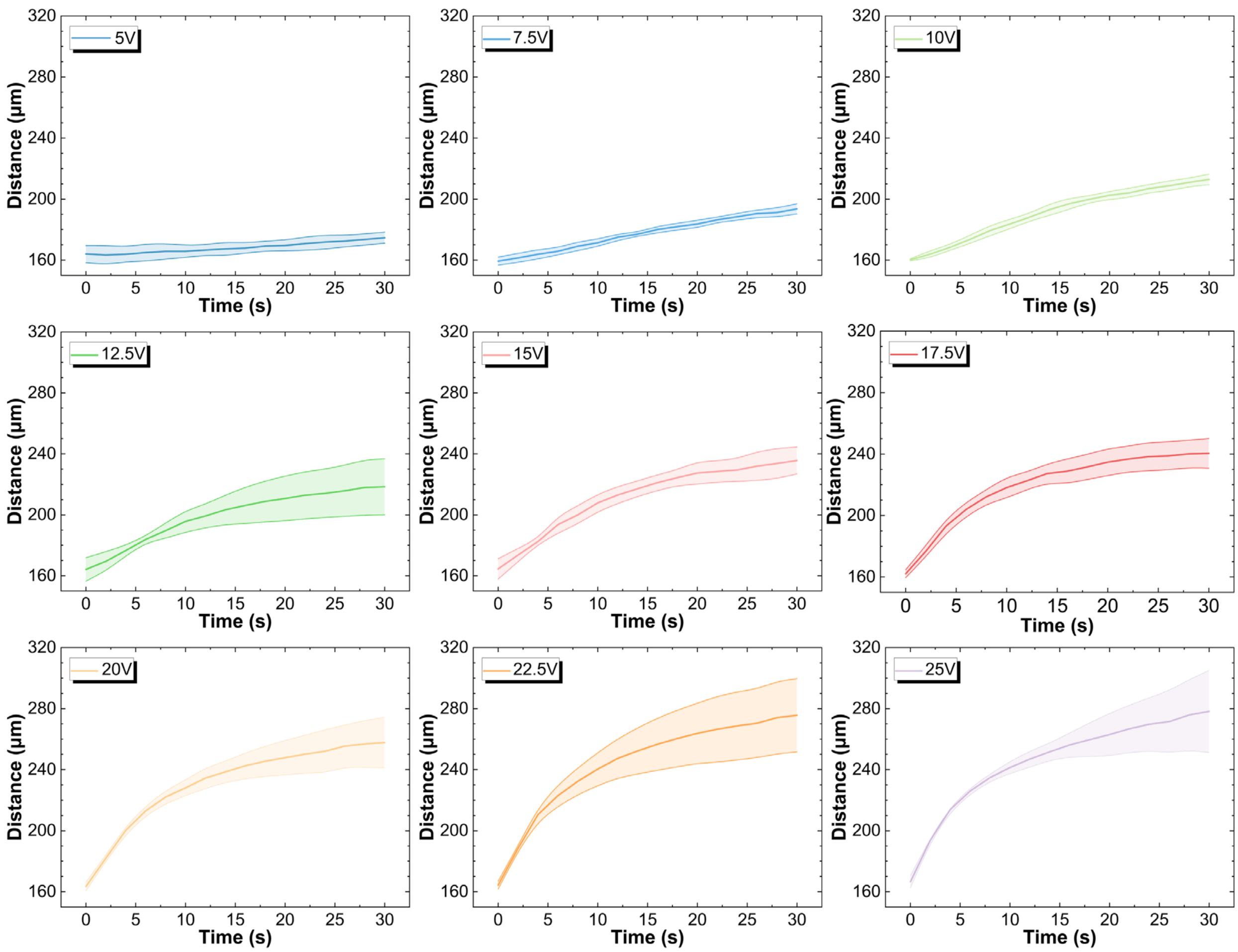

Fig. S6. Repulsion distance between micro-gears at different voltages over time.

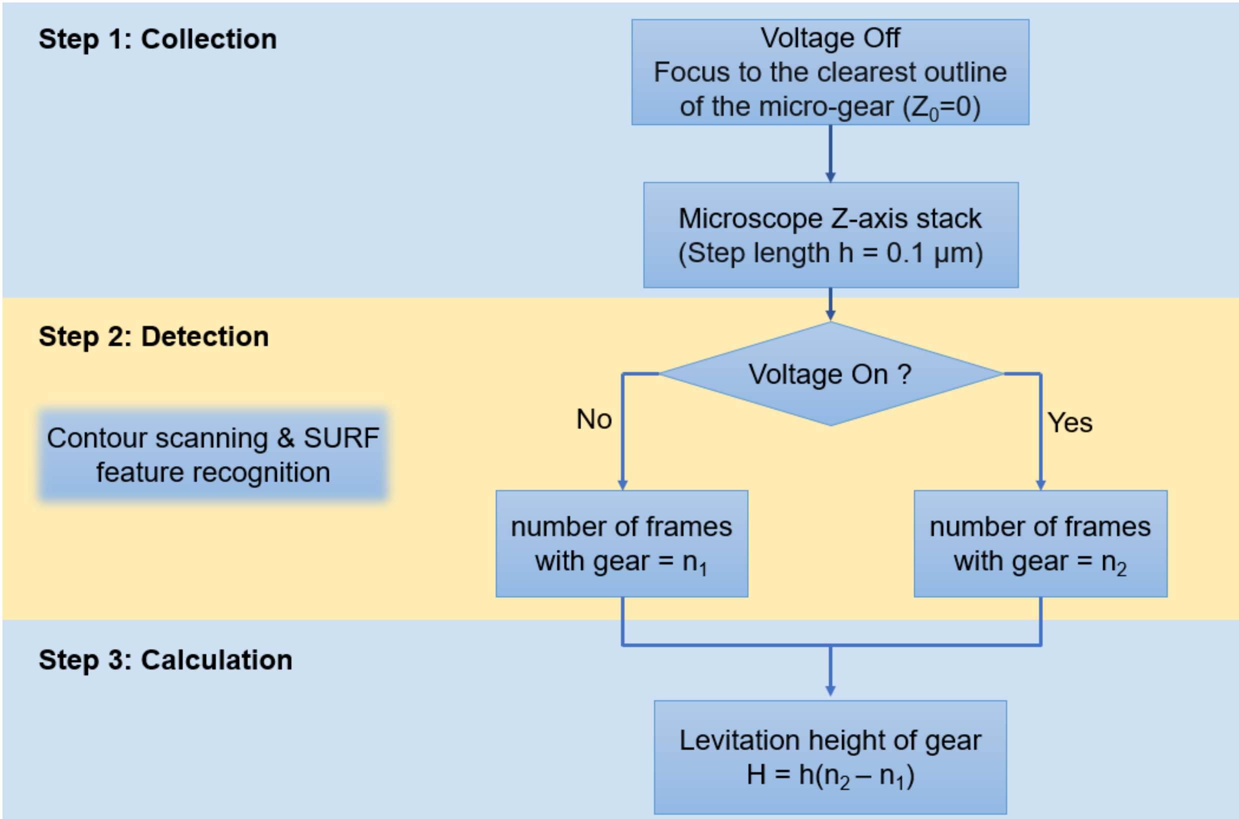

Fig. S7. Method for determining the uplifted height of micro-gear.

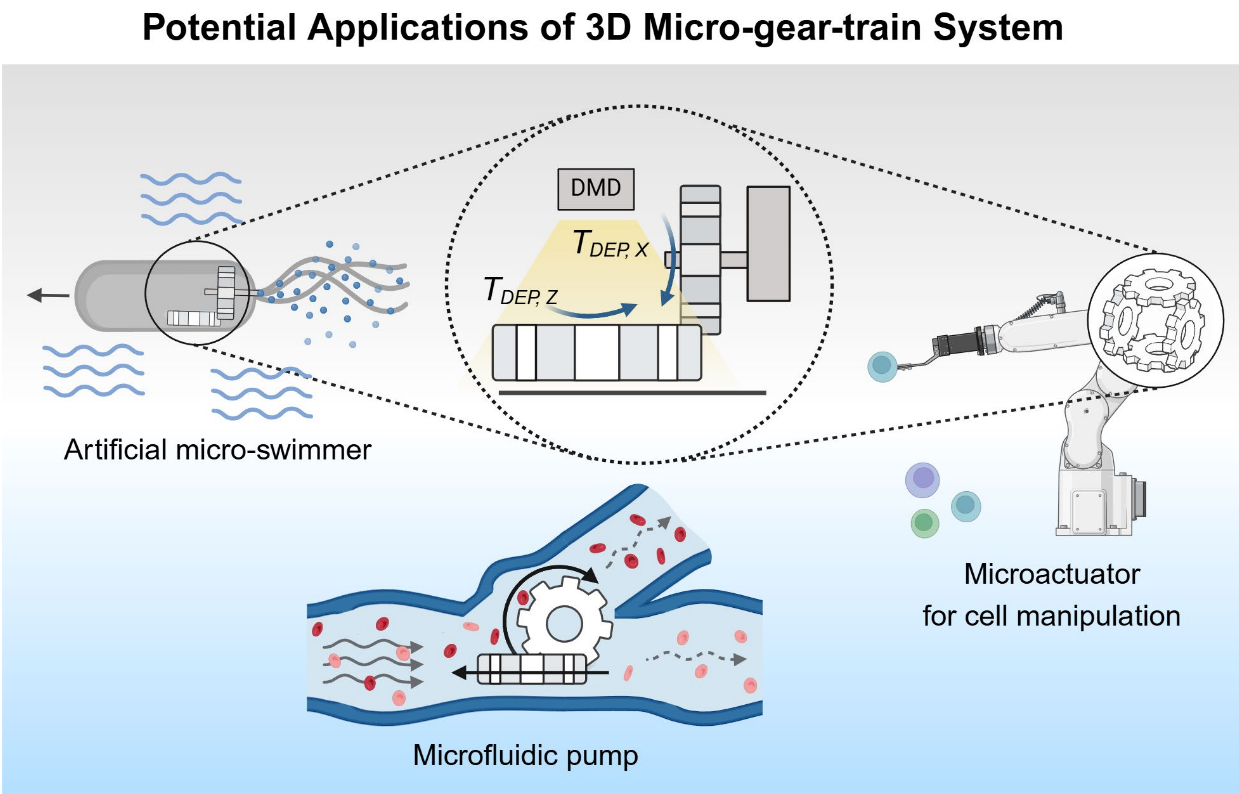

Fig. S8. Potential applications of 3D micro-gear train with capabilities for motion transfer across different planes, including as engines for article micro-swimmer, artificial joints for micro-actuator, and microfluidic pump.

Table S1. Simulation parameters of the OET device and micro-gear.

Parameters	Descriptions	Values
σ_{m}	Conductivity of liquid medium	5.5×10^{-6} S/m
$\sigma_{Si\text{-}illuminated}$	Conductivity of illuminated a-Si:H	1×10^{-4} S/m
$\sigma_{Si\text{-}dark}$	Conductivity of dark a-Si:H	1×10^{-6} S/m
$\sigma_{SU\text{-}8}$	Conductivity of SU-8	3.57×10^{-9} S/m
ε_{m}	Permittivity of liquid medium	80
$\varepsilon_{Si\text{-}illuminated}$	Permittivity of illuminated a-Si:H	11.7
$\varepsilon_{Si\text{-}dark}$	Permittivity of dark a-Si:H	11.7

ε_{SU-8}	Permittivity of SU-8	**4.1**
ρ_{SU-8}	Density of SU-8	**1200 kg/m^3**

Movie S1.

Schematic animation and experimental video showing the rotation of horizontal micro-gear and 2D co-planar micro-gear train (**Fig.2A, Fig.4F**).

Movie S2.

Schematic animation and experimental video showing the flip of micro-gear by pushing it using a circular light pattern (**Fig.2B**).

Movie S3.

Schematic animation and experimental video showing the rolling of micro-gear in the vertical plane (**Fig.2C**).

Movie S4.

Schematic animation and experimental video showing the controllable flip of micro-gear in limited space (**Fig.3A-B**).

Movie S5.

Experimental video showing the change of the micro-gear's flip axis.

Movie S6.

Schematic animation and experimental video showing the assembly and operation of 3D/cross-plane micro-gear train (**Fig.4C-E**).

Movie S7.

Experimental video showing the repulsion effect between micro-gears (**Fig.5D, Fig.S5D**).

Movie S8.

Schematic animation and experimental video showing the elevation of micro-gear after switching on the voltage (**Fig.6C**).